Physics of Fluids

Numerical simulation of hypersonic flat-plate boundary-layer blowing control ⊘

Zongxian Li (李宗贤) [ID] ; Meikuan Liu (刘美宽) [ID] ; Guilai Han (韩桂来) ✉ [ID] ; Dagao Wang (王大高) [ID] ;
Zonglin Jiang (姜宗林) [ID]

Check for updates

View Online   Export Citation

08 April 2024 03:06:28

AIP Publishing

Numerical simulation of hypersonic flat-plate boundary-layer blowing control

View Online   Export Citation   CrossMark

Zongxian Li (李宗贤),[1,2] (iD) Meikuan Liu (刘美宽),[1] (iD) Guilai Han (韩桂来),[1,2,a] (iD) Dagao Wang (王大高),[1,2] (iD)
and Zonglin Jiang (姜宗林)[1,2] (iD)

AFFILIATIONS

[1] State Key Laboratory of High Temperature Gas Dynamics, Institute of Mechanics, Chinese Academy of Sciences, Beijing 100190, China

[2] School of Engineering Science, University of Chinese Academy of Sciences, Beijing 100049, China

[a] Author to whom correspondence should be addressed: hanguilai@imech.ac.cn

ABSTRACT

Air-blowing is one of the techniques for active flow control and thermal protection system of hypersonic vehicles. Introducing air into the hypersonic boundary layer alters the cross-sectional profile of the boundary layer, thereby influencing the boundary-layer transition. This study investigates the active air-blowing control effects on the hypersonic flat-plate boundary layer under various blowing mass flow rates and incoming Mach numbers by solving the Reynolds-averaged Navier–Stokes equations with the Langtry–Menter four-equation transitional shear stress transport model. The study examined alterations in the blowing boundary-layer profiles under two conditions: natural and bypass transition, induced by different blowing flow rates. Blowing significantly alters the sonic line and boundary-layer profile characteristics, triggering blowing oblique shock and causing alterations in the instability mechanisms of the two transition states. A higher Mach number intensifies compressibility effects, stabilizing the boundary layer and leading to an increase in the thickness of the blowing boundary layer and air film.

I. INTRODUCTION

Hypersonic vehicles are prone to experience a laminar-turbulent transition in the boundary layer during operation,[1] leading to more complex and potentially more hazardous aerodynamic and aerothermal environments. This transition phenomenon has the potential to evolve into a pivotal concern, exerting influence over the outcome of the flight.[2] Due to varying hypersonic flight condition and diverse vehicle structures, the requirements for boundary-layer transition are complex and multifaceted. For instance, delaying boundary-layer transition can lead to a reduction in heat flux and facilitate enhanced thermal protection. Yet, at the same time, facilitating a transition to turbulence can enhance the ability to withstand boundary-layer separation and promote the admixture of fuel within the inlet of an air-breathing vehicle.[3] As a result, effective boundary-layer transition control methods must be employed to ensure the safe and efficient operation of hypersonic vehicle.

Exploring the boundary-layer stability has proven valuable for comprehending and investigating the transition mechanism of hypersonic boundary layers. The ultimate objective of investigating the transition mechanism and the laws governing it is to achieve precise prediction and boundary-layer transition control. Over the decades,

landmark studies in stability theory,[3–10] numerical simulation,[11–14] and wind tunnel experimentation[15–20] have significantly advanced the comprehension of the origins and mechanisms behind hypersonic boundary-layer transition problems. In their review of hypersonic boundary-layer transition issues from an overall design perspective, Li et al.[21] summarized the areas, causes, and negative impacts of boundary-layer transitions for reentry, gliding, and cruise vehicles. They emphasized the importance and urgency of adopting effective boundary-layer control methods to regulate boundary-layer transition for the safe and efficient operation of a vehicle.

Various boundary-layer control techniques are used in thermal protection systems (TPS),[22] inlet fuel injection,[23] suppression of shock wave/boundary-layer interactions (SW/BLI),[24] and control of the boundary-layer transition.[22,25–29] Boundary-layer control methods can be divided into active and passive according to whether external energy input is required.[27] Passive control methods include micro vortex generators (MVG),[30] roughness,[31] and porous media,[32] among other methods. Active control methods include wall heating/cooling,[33] magneto-hydrodynamic methods,[34] plasma jets,[35] and others.[6,25] Passive control methods principally involve installing specific shapes in fixed positions, which can achieve control effects tailored to specific
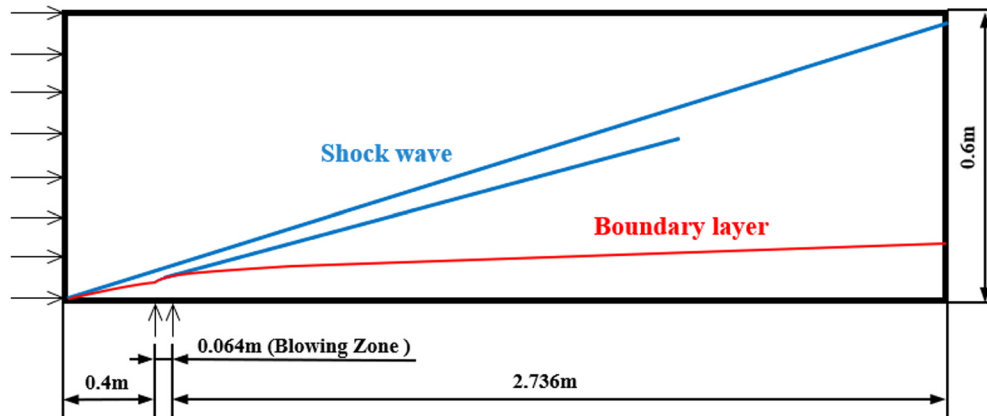
FIG. 1. Schematic diagram of the numerical model.

flowing conditions. Hypersonic flight vehicles, however, have a wide range of flight speeds and in broad airspace conditions, so that active control methods can achieve more accurate and appropriate control effects for different flow conditions.[25,36] In boundary-layer control technology, transition control is primarily achieved through two methods: altering the mean flow profile of the boundary layer and regulating the development and evolution of unstable waves within the boundary layer.[37] Blowing gas into the boundary layer is one of the active control technologies[25] and has numerous applications in hypersonic vehicles, such as transpiration cooling and the introduction of ablative gas into the boundary layer. Due to the addition of extra momentum and energy, this changes the boundary-layer basic flow and affects the transition. There is still some controversy about the influence of blowing on the stability of the boundary layer.[22] In early studies on blowing gas into the boundary layer,[38,39] it was generally believed that light gases would lead to an earlier transition, and heavier gases might lead to a delayed transition.[27] The analysis of linear stability theory (LST) shows that the most unstable mode of boundary-layer blowing is the Mack mode, and blowing will lead to an increase in the maximum growth rate of the most unstable frequency.[29] However, Schmidt et al.[28] found in their calculations a higher N-factor for the first mode and speculated that K–H instability is the dominant mechanism for the transition during blowing. On the other hand, Miró and Pinna[26] concluded that the previous transition laws apply only to non-continuous blowing. In the case of continuous blowing through porous media at the model's leading edge, light gases can stabilize the second mode, whereas heavy gases work against stability.

This paper presents numerical simulations of boundary-layer blowing on hypersonic flat plates based on experimental flow conditions obtained from the JF-12 hypersonic duplicate tunnel. The simulations were conducted for different blowing mass flow rates and different incoming flow Mach numbers to study the development of cross-sectional shape, edge height, and air film thickness of the basic flow in the boundary layer. The variation trend of the oblique shock wave intensity of the blowing and the additional disturbance brought about by the near-wall strong-blowing layer in the blowing region are compared. Additionally, the impacts on the evolution of sonic line height and disturbance region were assessed.

II. RESEARCH METHOD

A. Numerical model and boundary conditions

The calculation model used in this work is based on the physical model and experimental conditions of Liu et al.[19] in a large-scale flat plate boundary-layer transition experiment. As depicted in Fig. 1, the calculation domain spans 3.2 m in length and 0.6 m in height. Situated 0.4 m from the leading edge of the plate, the blowing zone extends 0.064 m in length. The viscous effect is strong near the wall, resulting in the generation of a boundary layer. Viscous forces within the boundary layer induce upward flow, resulting in a shock wave at the plate's leading edge. The introduction of gas into the boundary layer in the blowing region alters its shape and lifts its outer edge, generating an oblique shock wave. Based on these flow characteristics, the boundary conditions for the calculation model are established as follows. The incoming flow direction is on the left with a chosen supersonic inlet condition. The flow conditions are detailed in Table I, with Ma 7 condition being selected based on the experimental flow conditions of Liu et al.[19] In Table I, Ma is the Mach number, Re is the Reynolds number, T is the temperature, p is the pressure, and h is the enthalpy. The subscripts "0" and "∞" refer to the conditions in the nozzle reservoir and the freestream, respectively. To examine the impact of varying Mach numbers, two incoming flow conditions were selected with the same static temperature and unit Reynolds number, but different Mach numbers (7 and 8). The simulation of a flat plate employs an isothermal no-slip boundary condition on the lower surface of the model. The temperature at the wall, T_w, is 288 K. The blowing area, with a constant mass flow rate, is the inflow boundary, and its static temperature is the same as the wall temperature. Both the blowing gas and the incoming flow are ideal gases. The mass flow rate per unit length for the blowing is determined based on calibration in both an atmospheric

TABLE I. Boundary conditions of incoming flow.

Ma_∞	T_∞ (K)	Re_∞ (m^{-1})	T_0 (K)	p_∞ (Pa)	h_0 (J/kg)
7	232	1.25×10^6	2506	586	2.52×10^6
8	232	1.25×10^6	3202	513	3.22×10^6

TABLE II. The flow parameters of the blowing gas.

	$\dot{m}_0$	$\dot{m}_1$	$\dot{m}_2$	$\dot{m}_3$	$\dot{m}_4$
$\dot{m}$ (10^{-3} kg/s)	0	0.401	0.802	4.011	34.511
T_b (K)	288	288	288	288	288
h_b (J/kg)	2.89×10^5	2.89×10^5	2.89×10^5	2.89×10^5	2.89×10^5

TABLE III. Three grids used in the grid independence study.

Mesh	$N_y \times N_x$	Cell count
Sparse	450×5817	2.6×10^6
Medium	500×8537	4.3×10^6
Fine	$500 \times 14\,497$	7.2×10^6
Refine	$550 \times 14\,497$	8.0×10^6

pressure environment and the vacuum chamber of the JF-12 hypersonic duplicate tunnel (which utilized the same equipment as the experiment conducted by Liu *et al.*[19]). The flow parameters for each blowing condition are listed in Table II, where the subscript "b" denotes the blowing. The viscosity is computed using Sutherland's law. The right and upper sides of the incoming flow condition model serve as the flow outlet direction, with supersonic extrapolation applied as the boundary condition.

B. Numerical methods

In this work, the boundary-layer blowing control process is simulated using the two-dimensional (2D) compressible ideal gas Reynolds-averaged Navier–Stokes (RANS) equations, which are solved using the finite volume method. The spatial discretization is reconstructed by second-order TVD (total variation diminishing) of multidimensional polynomial interpolation, and the numerical flux at the

interface is calculated by Harten–Lax–van Leer contact (HLLC). The viscous flux is computed using the simple second-order average of all vertex polynomials. The dual time stepping method is used for time integration. In order to investigate the phenomena of transition and turbulence, this work adopts the Langtry–Menter four-equation transition stress shear transport model (γ-Re$_\theta$) that introduces the vortex Reynolds number to solve for the boundary-layer-related quantities locally.[40] This transition model establishes a correlation between physical quantities such as local turbulence intensity and pressure gradient with the momentum-thickness Reynolds number for transition. It determines the transition location by calculating the ratio of the local vorticity Reynolds number to the critical thickness Reynolds number.[3] This model has been extensively applied in the investigation of hypersonic boundary-layer transition. Numerical experiments[41–44] focused on hypersonic flat plate and cone models to verify this transition model's capability in predicting aerodynamic parameters such as wall heat flux and pressure. It substantiated its capacity to simulate the physical phenomena of hypersonic boundary-layer transition. Cheng *et al.*,[45] Yan *et al.*,[46] and Zhang *et al.*[47] made further modifications and calibrations to the transition model and achieved favorable numerical simulation results.

C. Independence verification and code validation

To ensure that the numerical results are independent of grid scale, this study calculated the plate boundary layer using four different grid sizes for the *Ma* 7-$\dot{m}_0$ condition. Table III lists the specifications of the four grid sets.

Figure 2 presents the profiles of temperature and velocity boundary layers at various locations along the flow, computed using four different grid sets. The horizontal axis represents the dimensionless temperature or velocity, while the vertical axis represents the normal coordinate of the flow field. For a sparse grid, the boundary layer is calculated to have a lower peak temperature and experiences a faster increase in temperature as well as velocity after reaching its peak. Additionally, the sparser grid leads to a thinner calculated boundary layer. As the gird is refined, the temperature and velocity boundary-
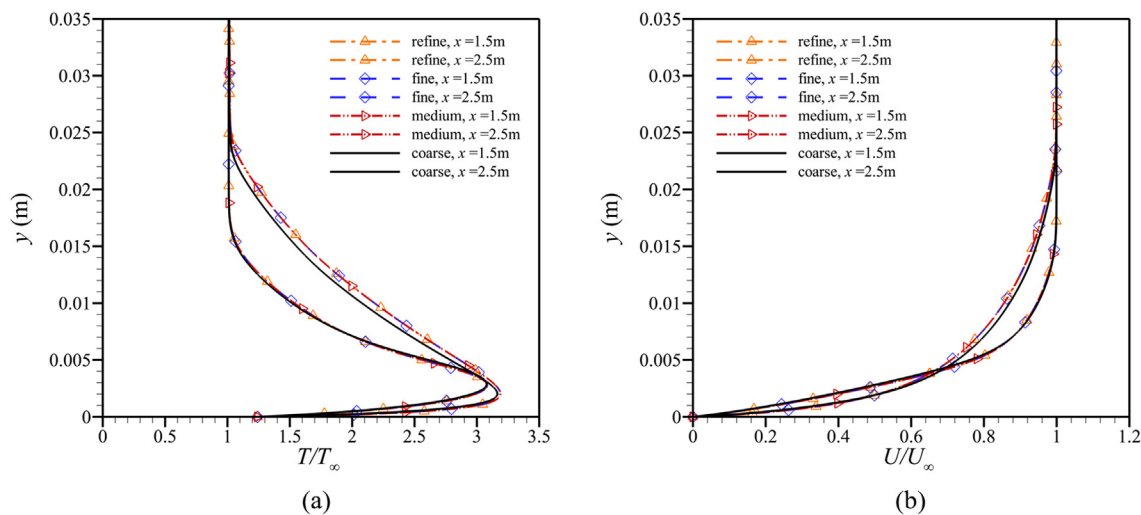
FIG. 2. (a) Dimensionless temperature boundary-layer section and (b) dimensionless velocity boundary-layer section as functions of distance from wall for different grid sets.
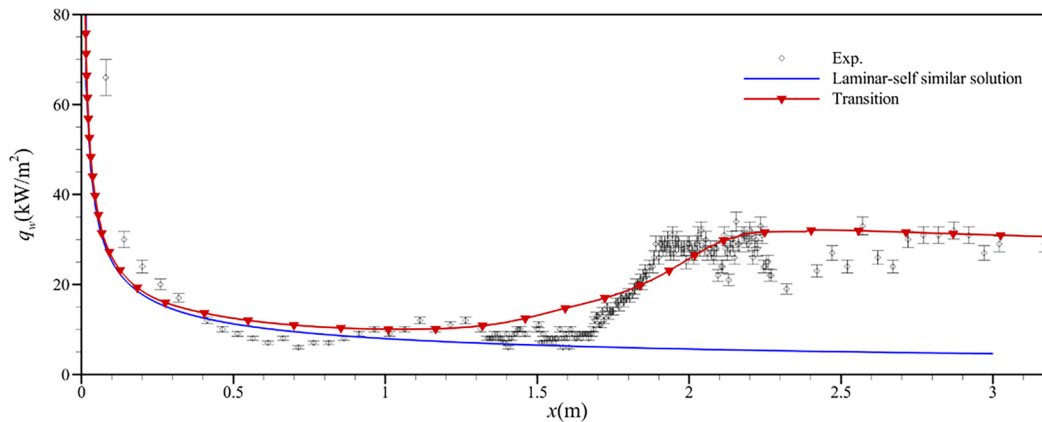
FIG. 3. Wall heat flux verification.

layer curves of each flow direction gradually become consistent. Taking into account both accuracy and efficiency of the calculations, this work selects medium mesh for computation.

In this study, the computational program is validated using the results of flat-plate boundary-layer transition wind tunnel experiments conducted by Liu *et al.*[19] The flow conditions are the following: Mach number $Ma_\infty = 5.85$, unit Reynolds number $Re_\infty = 0.91 \times 10^6$ m^{-1}, and total temperature $T_0 = 1752$ K. Figure 3 compares measured heat flux distribution with the numerical results. It also shows the laminar heat flux in the boundary layer obtained from the self-similar solution[48] of the plate laminar boundary layer. In Fig. 3, the x-axis represents the flat flow direction coordinate and the y-axis represents the wall heat flux q_w.

The calculation results accurately reflect the evolution process of the flat boundary layer from laminar to turbulent flow, as shown in Fig. 3. In the laminar flow region upstream of a flat plate, the heat flux decreases due to the increasing thickness of the boundary layer. Subsequently, as the boundary-layer transitions, the heat flux begins to increase. After the boundary layer develops into a fully turbulent flow, the heat flux reaches its peak, then gradually decreases. The calculated wall heat flux on the plate boundary layer agrees well with both the wind tunnel experiments and the self-similar solution of the laminar boundary layer, verifying the validity of the computational program and its suitability for subsequent research.

III. RESEARCH RESULTS

This section delves into the influence of variations in blowing mass flow rate and the incoming flow Mach number on the flat-plate boundary layer. The comparison and analysis are performed for the flow-field structure, transition characteristics, and boundary-layer profile adjacent to the blowing region. Through this methodology, the investigation examines the effects and mechanisms governing boundary-layer control via blowing, as operational conditions change during the flight of the hypersonic vehicle.

A. Effect of different blowing mass flow rates

This section reports an investigation of the diverse control effects achieved by distinct blowing mass flow rates under consistent incoming flow conditions through active blowing control. The report commences with an examination of flow-field structures in the vicinity of

the blowing region, introducing the distinct characteristics induced by the blowing process. Subsequently, the evolution of heat flux on the flat plate is analyzed to elucidate the boundary-layer transition characteristics resulting from different flow rates. Finally, distinct boundary-layer profiles for each mass flow rate are analyzed based on their respective transition characteristics.

1. Flow structure

This subsection examines the impact of varying blowing mass flow rates on the evolution of the flow-field structure for the incoming condition of Ma 7. The density gradient is depicted in Fig. 4 near the blowing region under conditions of varying mass flow rates. The solid red line represents the sonic line, reflecting the subsonic region where the second mode propagates[4] The blue solid line represents the streamline formed by the blowing gas, which is used to describe the trajectory of the gas injected into the boundary layer. The brown dot-dash line indicates the boundary layer's outer edge. After the blowing shock wave, alterations in velocity, temperature, and pressure. Therefore, the outer edge of the boundary layer is defined based on the location where the dimensionless total enthalpy of the boundary layer reaches 0.99.[49] The total enthalpy is nondimensionalized based on the incoming flow's total enthalpy. In the following equation, where h_0 is the dimensionless total enthalpy at the boundary layer's outer edge, h_0^* is the total enthalpy of the flow field, and $h_{0\infty}^*$ is the total enthalpy of the incoming flow:

$$h_0 = \frac{h_0^*}{h_{0\infty}^*} = \frac{T/(\gamma-1) + 0.5(u^2 + v^2)Ma_\infty^2}{1/(\gamma-1) + 0.5Ma_\infty^2} = 0.99. \quad (1)$$

As air is blown into the boundary layer, a section of the boundary layer is lifted and its thickness increases as the mass flow rate increases. An oblique shock wave is generated above the boundary layer as its edge shape changes, and its intensity also increases with the escalation of the flow rate. The blowing creates an air film covering the wall of the blowing zone as well as downstream. For the low mass flow rate conditions of $\dot{m}_1 = 0.401 \times 10^{-3}$ kg/s and $\dot{m}_2 = 0.802 \times 10^{-3}$ kg/s, the influence of blowing air on the mean flow is negligible. The gas film established by those two conditions remains close to the wall. The boundary-layer height and the sonic line height closely resemble those of the non-blowing condition. The marginal increase in the
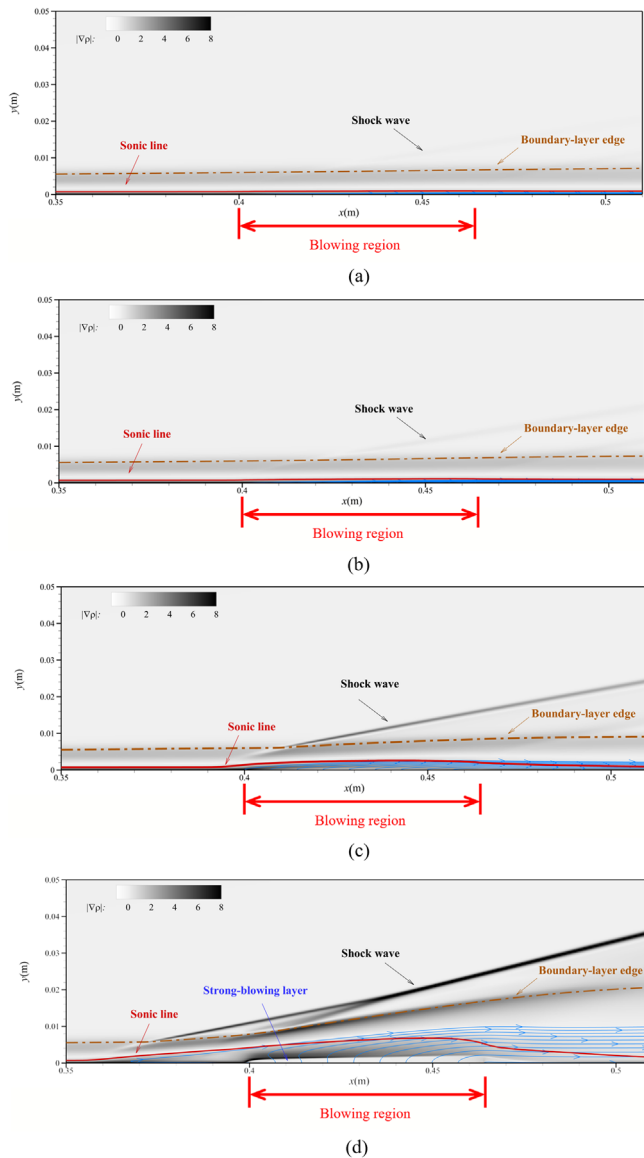
FIG. 4. Density gradient for different blowing mass flow rates: (a) $\dot{m}_1 = 0.401 \times 10^{-3}$ kg/s, (b) $\dot{m}_2 = 0.802 \times 10^{-3}$ kg/s, (c) $\dot{m}_3 = 4.011 \times 10^{-3}$ kg/s, and (d) $\dot{m}_4 = 34.511 \times 10^{-3}$ kg/s.

boundary-layer edge oblique shock above the blowing region is weak and barely visible in the Fig. 4. When the mass flow rate of the blowing air is insufficient, the air film is deflected downstream in the blowing area. For a large mass flow rate of $\dot{m}_4 = 34.511 \times 10^{-3}$ kg/s, the blowing generates a large enough pressure gradient to cause backflow upstream of the blowing region. This results in an earlier rise of the outer edge shape of the boundary-layer upstream, generating a series of compression waves that converge to form an oblique shock above the blowing region, as shown in Fig. 4(d). Above the blowing region, a zone with zero temperature gradient and zero x component of velocity becomes evident, distinctly forming a "strong-blowing layer."

In a hypersonic flat plate boundary layer without blowing flow, the pressure change is minimal. However, when gas is injected into the boundary layer, the pressure distribution within the boundary layer is altered. The alteration of the pressure distribution within the boundary layer and the interaction introduced by the oblique shock wave will further influence the evolution of the disturbance wave. Figure 5 illustrates the pressure changes near the blowing region for four different blowing flow rates. The blowing increases the static pressure of the boundary layer above the blowing area. Additionally, the oblique shock wave of the blowing causes an increase in pressure beyond the shock wave, forming a high-pressure strip with a width similar to the length of the blowing zone. As the mass flow rate increases, the blowing gas induces a greater pressure increase. Figure 6 displays the wall pressure for various blowing mass flow rates. The adverse pressure gradient in the subsonic region near the wall causes the region in which the pressure is changing to expand upstream of the blowing region. The wall pressure reaches its maximum value beyond the blowing oblique shock wave within the blowing region. As the ejected gas expands downstream of the blowing region, it causes a pressure drop that eventually approaches the non-blowing flat plate wall pressure far downstream. An increase in the flow rate leads to an expansion of the pressure disturbance range within the boundary layer near the blowing region.

The oblique shock causes an abrupt change in temperature and velocity above the boundary layer. Table IV shows the effect of different blowing mass flow rates on shock intensity. The angle β between the oblique shock wave and the wall is identified by the maximum flow pressure gradient. As the mass flow rate increases, the included angle of the oblique shock wave increases, and the intensity of the shock wave strengthens. This leads to stronger viscous-inviscid interaction near the boundary layer and affects the boundary-layer transition.

To ensure a uniform blowing over a large surface, it is a common practice to discharge the air perpendicularly to the wall through a porous medium. Given the constant mass flow rate and static temperature of the blowing air, the velocity distribution in the blowing region can be determined based on the wall pressure using the ideal gas state equation. The normal velocity distributions of the blowing region for different mass flow rates are shown in Fig. 7. An increase in the mass flow rate implies that air is injected into the boundary layer with a higher velocity. In Fig. 6, the wall pressure distribution characteristics in the blowing region are depicted. The peak of the wall pressure in the blowing region occurs at the foot of the blowing shock. Beyond the peak point, the blowing experiences expansion, leading to a decline in pressure. Consequently, the normal velocity of the blowing decelerates initially decelerates and then undergoes acceleration due to expansion.

2. Transition characteristic

The influence on the boundary-layer transition is discussed based on the development of wall heat flux downstream of the blowing region. To begin, an analysis is conducted regarding the evolution of wall heat flux near the blowing region for Ma 7. As shown in Fig. 8, the abscissa is the coordinate of the plate position, while the ordinate denotes the wall heat flux (q_w). For both lower and higher mass flow rates, the laminar boundary layer thickens continuously upstream of the blowing region, resulting in a rapid decrease in heat flux. Within the blowing region, heat flux further declines due to the cooling effect of the blowing gas and the lifting of the boundary layer by the blowing. Downstream of the blowing region (as shown in Fig. 9), the
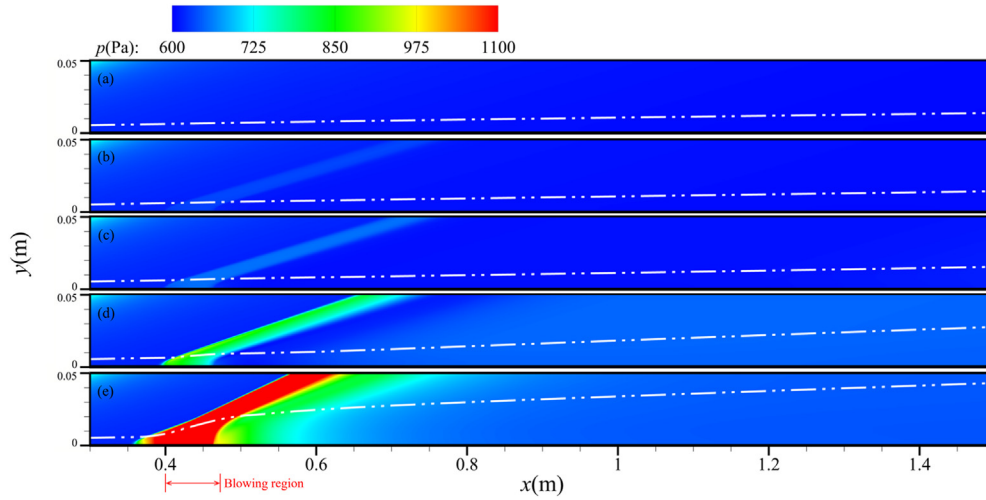
FIG. 5. Static pressure for (a) $\dot{m}_0 = 0$, (b) $\dot{m}_1 = 0.401 \times 10^{-3}$ kg/s, (c) $\dot{m}_2 = 0.802 \times 10^{-3}$ kg/s, (d) $\dot{m}_3 = 4.011 \times 10^{-3}$ kg/s, and (e) $\dot{m}_4 = 34.511 \times 10^{-3}$ kg/s.
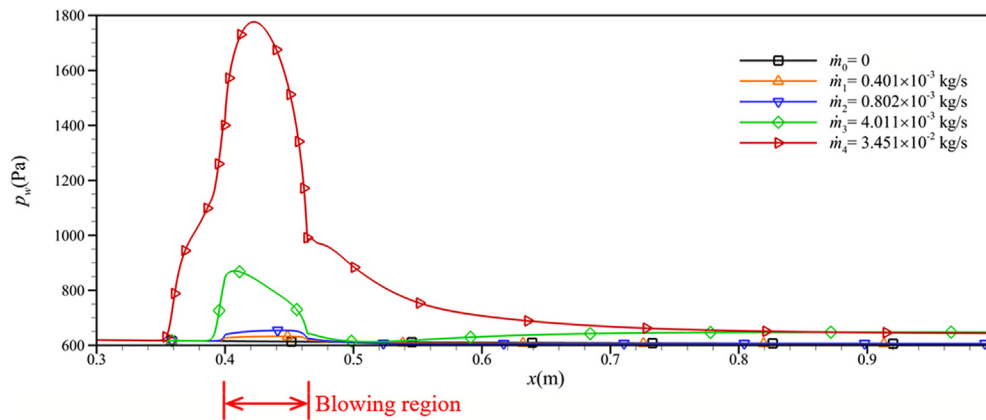

FIG. 6. Wall pressure for different blowing mass flow rate.

TABLE IV. Oblique shock wave angles caused by different mass flow rates.

$\dot{m}$ (10^{-3} kg/s)	0.401	0.802	4.011	34.511
β (°)	8.8	8.9	9.9	13.1

dimensionless temperature profile of the boundary layer rises as it regains self-similarity (refer to Sec. III, "Boundary-layer Profile Shapes"). So, a boundary-layer transition occurs after heat flux close to that of laminar flow is restored downstream of the blowing region. The transition causes heat flux to rise until it develops into a turbulent boundary layer. However, when the mass flow rate increases to $\dot{m}_3 = 4.011 \times 10^{-3}$ kg/s, the type of boundary-layer transition changes. The heat flux downstream of the blowing region no longer reverts to laminar but immediately increases to turbulent heat flux. In contrast, for the high mass flow rate of $\dot{m}_4$, the trend of heat flux change is roughly consistent with other conditions. However, several notable features occur: first, the formation of a recirculation zone above the blowing zone due to a reverse pressure gradient, causing the boundary layer to rise prematurely and heat flux to drop rapidly around $x = 0.35$ m; second, an increase again of heat flux due to the deceleration of flow within the recirculation zone; and third, formation of a strong-blowing layer within the blowing region where heat flux is reduced to zero. Downstream of the blowing area, a bypass transition occurs and heat flux increases rapidly. Furthermore, the increase in the mass flow rate enhances the cooling effect of the blowing, resulting in the formation of a longer low-heat-flux region at the $\dot{m}_4$ condition and forcing the upward movement of the location where heat flux increases downstream. Simultaneously, this also leads to a reduction in the heat flux increment at the $\dot{m}_4$ condition after transition.

The above analysis reveals the different wall heat-flux-evolution characteristics downstream of the blowing region, which can be used to compare how the blowing mass flow rate affects the boundary-layer transition. The analysis of the variation in transition position with mass flow rate is based on the wall heat flux characteristics
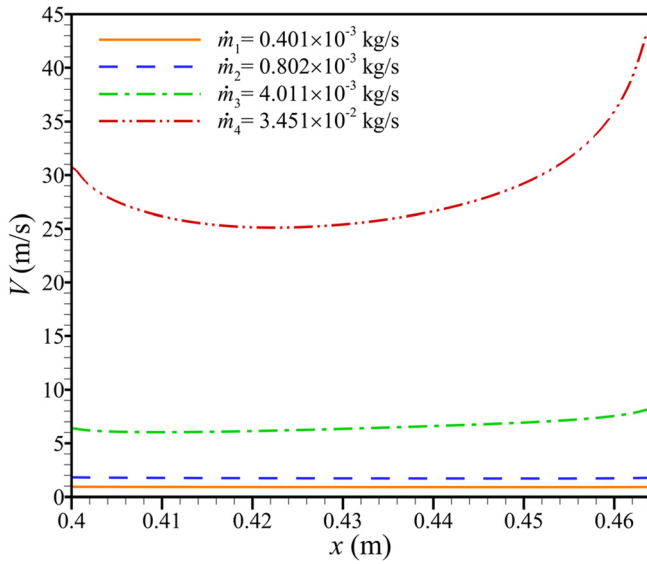
FIG. 7. The normal velocity of the blowing region for different blowing mass flow rate.

downstream of the blowing region, as depicted in Fig. 9. The x-axis is in the flow direction coordinate, while the y-axis is in the direction of wall heat flux. This work aims to quantify the influence of blowing mass flow rate on the transition trend by examining the variation of the heat flux along the wall. Since the heat flux in the numerical solution changes continuously, there is no distinct heat flux takeoff point. Therefore, this work draws upon the CFDR method proposed by Miro et al.[50] to define the transition position as the intersection point of two curves. One curve is derived from the laminar self-similar solution of heat flux. The other curve is a linear regression line based on the numerical solution of wall heat flux. Building upon the original CFDR method, the linear regression range is explicitly specified as the section of the heat transfer curve that rises from 50% to 100% of its peak value in the turbulent regime. Comparing different mass flow rates, the transition position moves upstream as the mass flow rate increases and there are three types of changes in the flow state. First, as the mass flow rate increases from zero to 0.802×10^{-3} kg/s, the boundary layer maintains a natural transition, and the transition position continues to move forward. The value of x_{tr} decreases from 1.80 m without blowing to 1.49 m with a blowing mass flow rate of $\dot{m}_1$ and further to 1.13 m with a blowing mass flow rate of $\dot{m}_2$. As the mass flow rate increases twofold from $\dot{m}_0$ to $\dot{m}_2$, the distance Δx_{tr} that the transition position moves forward increases from 0.31 to 0.36 m. This indicates that the
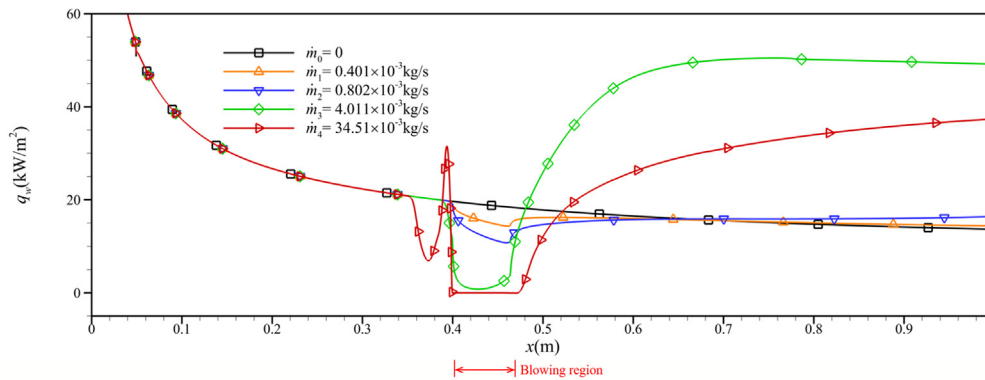

FIG. 8. The evolution of wall heat flux near the blowing region for various blowing mass flow rates.
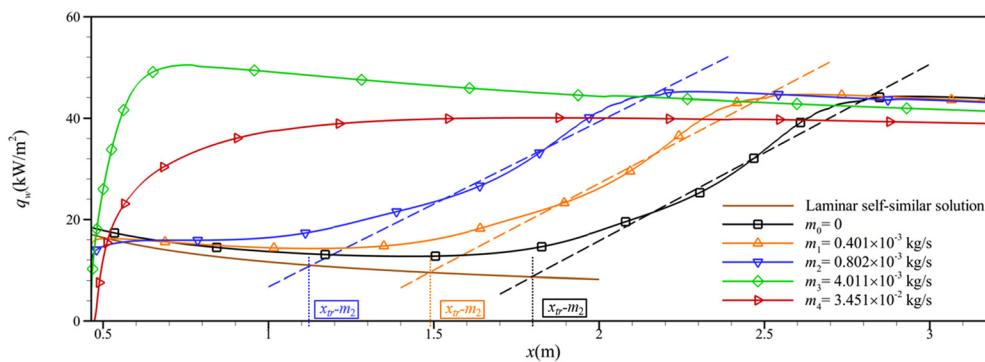

FIG. 9. Wall heat flux for various blowing mass flow rates.

TABLE V. Ratio of gas film to boundary-layer thickness.

$\dot{m}$ (10^{-3} kg/s)	0.401	0.802	4.011	34.511
Thickness ratio (%)	7.1	11.4	32.5	57.9

transition spatial position does not vary linearly with the blowing mass flow rate. Moreover, the forward trend of the transition position accelerates as the blowing mass flow rate increases proportionally. Second, when the flow rate increases further to $\dot{m}_3 = 4.011 \times 10^{-3}$ kg/s, a bypass transition occurs immediately behind the blowing zone, and the heat flux rapidly rises to turbulent heat flux. Third, when the mass flow rate continues to increase to $\dot{m}_4 = 34.511 \times 10^{-3}$ kg/s, although there is still a bypass transition downstream of the blowing area, its heat flux decreases as a whole compared with $\dot{m}_3$.

The shift of wall heat flux from the second type to the third type is due to the cooling effect of blowing air. After being ejected from the blowing area, the gas is deflected into the streamwise direction, forming a cooling gas film that covers the wall within the boundary layer. The thickness of this air-film will affect the downstream turbulent wall heat flux. In this work, the thickness of the air film is measured by the distance between the streamline originating at the front edge of the blowing zone and the wall. Table V shows the ratio of air film thickness to boundary-layer thickness for different mass flow rates at $x = 0.464$ m (the end of the blowing region). At low flow rates, the cooling air film becomes thinner. The heat flux of the turbulent boundary layer at flow rate $\dot{m}_1 = 0.401 \times 10^{-3}$ kg/s or $\dot{m}_2 = 0.802 \times 10^{-3}$ kg/s shows a little change compared to the boundary layer without blowing, combining with Fig. 9. As the blowing mass flow rate increases, the gas film's thickness also rises and occupies a larger proportion of thickness in the boundary layer. Relative to other cases, the case with the maximum mass flow, the $\dot{m}_4$ condition, has a thicker gas film downstream of the blowing area, forming a "buffer zone" that slows down the temperature rise near the wall, resulting in a lower wall heat flux.

The intermittency factor, which represents the chaotic nature of turbulence within the boundary layer, is defined as the fractional duration of turbulent flow at a specific location. So, according to the Humble definition,[51] within fully turbulent domains, the intermittency factor γ equals 1, whereas within non-turbulent domains, γ is zero. In the absence of air blowing, the intermittency factor distribution for a typical flat-plate boundary layer is shown in Fig. 10(e). Within the laminar-flow region, this factor changes gradually along the direction normal to the wall and its thickness is equal to that of the boundary layer. After transitioning to turbulent flow, the intermittency factor rapidly increases to 1 near the wall. A wake line with low intermittency factor forms on the outer edge of the boundary layer and gradually dissipates along the flow direction. The transition position moves upstream and the transition advances for the low mass flow rates $\dot{m}_1 = 0.401 \times 10^{-3}$ kg/s and $\dot{m}_2 = 0.802 \times 10^{-3}$ kg/s. This leads to an increase in the intermittency factor along the normal gradient at a position closer to upstream, resulting in an earlier formation of the wake line. As the mass flow rate continues to increase, the low intermittency factor near the blowing region immediately breaks down, and the low intermittency factor zone near the wall downstream of the blowing region disappears. The sudden change in the intermittency factor distribution also reflects the shift in boundary-layer transition type to bypass transition. Especially noticeable when the mass flow rate reaches 34.511×10^{-3} kg/s, the adverse pressure gradient and oblique shock wave interaction exert a significant influence on the bypass transition. The inception point of disintegration advances to the recirculation zone. Concurrently, the intermittency factor wake line ruptures at the location where the inviscid-viscous interaction of the blowing oblique shock wave takes place above the blowing region.

Turbulent kinetic energy reflects the magnitude of velocity fluctuations within the boundary layer. Figure 11 illustrates the distribution of turbulent kinetic energy in the boundary layer at varying mass flow rates. In the case a natural transition under low blowing control, turbulent kinetic energy quickly peaks along the normal direction after leaving the wall in the turbulent boundary layer, and then gradually
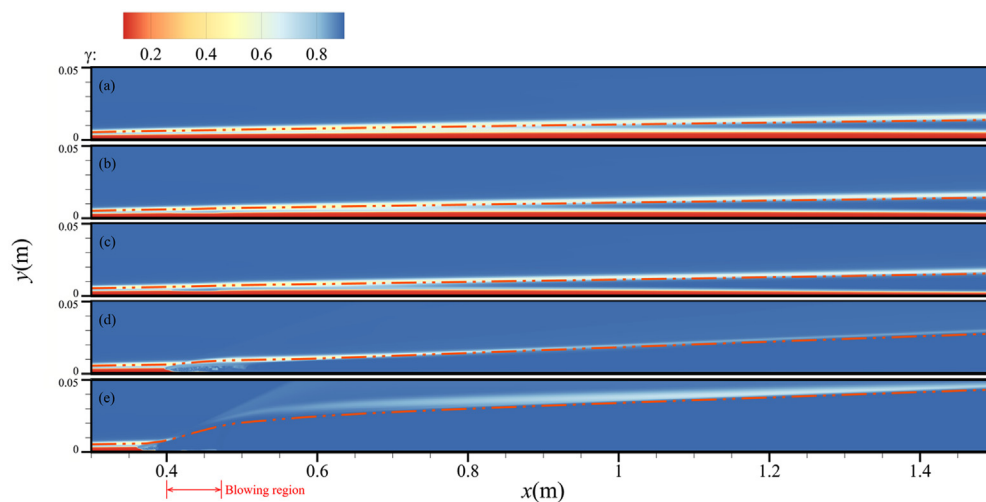

FIG. 10. Intermittency factor for different blowing mass flow rates: (a) $\dot{m}_4 = 34.511 \times 10^{-3}$ kg/s, (b) $\dot{m}_3 = 4.011 \times 10^{-3}$ kg/s, (c) $\dot{m}_2 = 0.802 \times 10^{-3}$ kg/s, (d) $\dot{m}_1 = 0.401 \times 10^{-3}$ kg/s, and (e) $\dot{m}_0 = 0$.
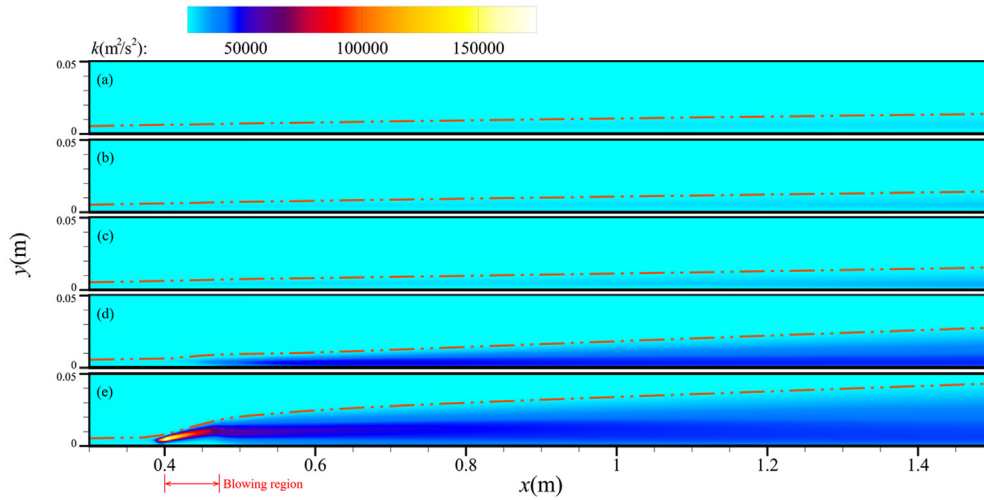
FIG. 11. Turbulent kinetic energy for different blowing mass flow rates: (a) $\dot{m}_4 = 34.511 \times 10^{-3}$ kg/s, (b) $\dot{m}_3 = 4.011 \times 10^{-3}$ kg/s, (c) $\dot{m}_2 = 0.802 \times 10^{-3}$ kg/s, (d) $\dot{m}_1 = 0.401 \times 10^{-3}$ kg/s, and (e) $\dot{m}_0 = 0$.

decreases as it continues to approach the outer edge of the boundary layer. A low flow rates, the region of high turbulent kinetic energy is concentrated in the downstream turbulent boundary-layer region and migrates upstream as the mass flow rate increases, with its peak value being smaller than that for high mass flow rate conditions. The movement of the peak value of turbulent kinetic energy during the increase in the blowing mass flow rate from low to high shows, on the one hand, that there is a difference in the dominant mechanism between the blowing control natural transition and the bypass transition; and, on the other hand, it further emphasizes the significance of oblique shock wave disturbances to the boundary layer. At the maximum flow rate studied, $\dot{m}_4$, the region of high turbulent kinetic energy has advanced to the upstream air-blowing region. The peak value of turbulent kinetic energy is transferred to the intersection between the oblique shock

wave of the blowing and the outer edge of the boundary layer; it then gradually diminishes as it progresses downstream.

3. Boundary-layer profile shapes

With the objective of addressing the $\dot{m}_1$ and $\dot{m}_2$ conditions that lead to natural transitions in low mass flow rates, the variation in the self-similarity of dimensionless temperature and velocity profiles near the blowing area is analyzed here. Figures 12 and 13 illustrate the profiles of the dimensionless temperature boundary layer at various positions in the flow direction, in proximity to the blowing region. These positions are located at $x = 0.36$–0.56 m, with mass flow rates corresponding to conditions $\dot{m}_1$ and $\dot{m}_2$. The x-axis marks the dimensionless temperature, while the y-axis provides the normal coordinate of the self-similar transformation.
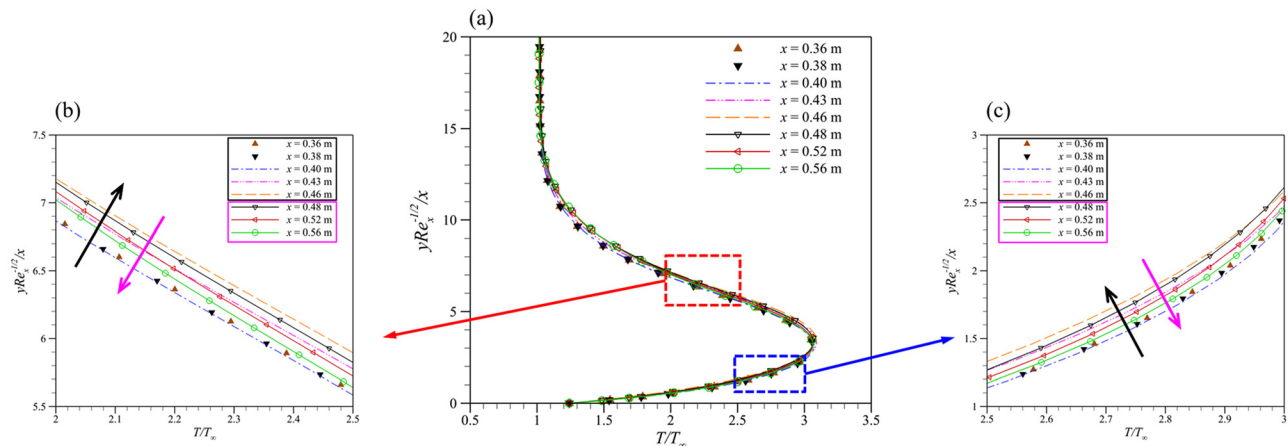

FIG. 12. Dimensionless boundary-layer temperature profiles for the blowing mass flow rate $\dot{m}_1 = 0.401 \times 10^{-3}$ kg/s: (a) overall view and (b) and (c) magnified views of specific areas.
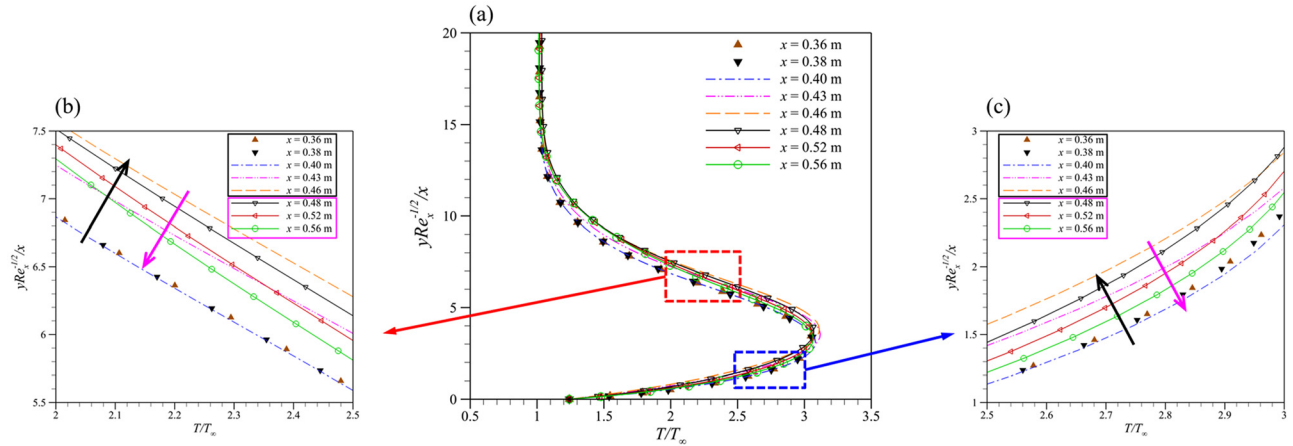
FIG. 13. Dimensionless boundary-layer temperature profiles for the blowing mass flow rate $\dot{m}_2 = 0.802 \times 10^{-3}$ kg/s: (a) overall view and (b) and (c) magnified views of specific areas.

Comparing Figs. 12(a) and 13(a), one can see that the boundary-layer section retains some kind of laminar self-similarity for mass flow rates $\dot{m}_1 = 0.401 \times 10^{-3}$ kg/s and $\dot{m}_2 = 0.802 \times 10^{-3}$ kg/s. However, as the flow rate increases, it gradually deviates from self-similarity and the thickness of the boundary layer gradually increases. In Figs. 12(b) and 12(c), as well as Figs. 13(b) and 13(c), where locally magnified images at identical coordinates are depicted, the black and magenta boxes in the legend represent the blowing area and its downstream region, respectively. On the one hand, the locally magnified image distinctly illustrates that the dimensionless temperature boundary-layer profiles at various positions become increasingly discrete as the mass flow rate increases. On the other hand, the arrows indicate the change in temperature profile along the flow direction. The black arrows show an upward trend in the blowing region's temperature profile as it moves downstream. In contrast, magenta indicates that the temperature boundary layer changes in the opposite direction downstream of the blowing area. The boundary-layer profile moves downward along the flow direction, indicating a tendency to restore laminar flow's self-similarity. Additionally, it is noteworthy that the dimensionless temperature boundary-layer profiles still exhibit strong self-similarity at $x = 0.36$–0.40 m upstream of the blowing region.

At the bypass transition, caused by the two large mass flow rates $\dot{m}_3$ and $\dot{m}_4$, the flow field near the blowing zone undergoes significant changes. For the bypass transition caused by conditions $\dot{m}_3$ and $\dot{m}_4$, a recirculation zone and oblique shock wave are generated near the blowing area. These cause the boundary layer to lose its laminar self-similarity, as clearly depicted in Fig. 14 Consequently, an analysis in conjunction with the flow field characteristics is necessary.

A thicker strong-blowing layer forms at the wall of the blowing region as shown in Fig. 4(d). This is evident in Fig. 14 which displays the dimensionless streamwise velocity and temperature boundary-layer profile. The double-dotted lines in the figure map zero velocity and zero temperature. The strong-blowing layer exhibits very little changes in temperature and streamwise velocity along the normal direction near the wall of the blowing region. The formation of the strong-blowing layer is similar to creating a forward step on the wall, which further affects the morphology of the boundary layer. The

negative streamwise velocity in Fig. 14(b) confirms the presence of a recirculation zone.

By analyzing the changes in sonic lines for various blowing conditions, the evolution of the disturbance area can be examined. Figure 15 shows the heights of sonic lines for different blowing conditions. Upstream of the blowing region, the height of the sonic line is essentially identical to that of the non-blowing condition ($\dot{m}_0$). However, under the condition $\dot{m}_4 = 34.511 \times 10^{-3}$ kg/s, the sonic line exhibits an earlier rise due to reversed flow. Unlike the monotonic change in boundary-layer height along the flow direction, near the blowing region, the cooling effect of blowing air causes the temperature profile curve to rise. This results in an upward shift of the sonic line and an expansion of the subsonic region. The boundary layer tends to restore self-similarity at low flow rates and the bypass transition at high flow rates both lead to a faster increase in temperature along the normal direction than in the blowing region. So the height of the sonic line decreases behind the blowing region. For a change from $\dot{m}_1 = 0.401 \times 10^{-3}$ kg/s to $\dot{m}_2 = 0.802 \times 10^{-3}$ kg/s, the temperature gradient increases due to the advance of the transition position caused by the increase in the mass flow rate. As a result, the height of the sonic line decreases gradually with an increase in the mass flow rate during the downstream progression. In the far downstream, all blowing conditions develop into a fully turbulent boundary layer and the height of the sonic line tends to be the same. In the hypersonic boundary layer, the dominant second mode and its high-order harmonic waves are constantly reflected between the sonic line and the wall, and propagate forward.[4] The rise of the sonic line will lead to changes in the frequency of unstable waves, which can greatly affect the evolution of the disturbance mechanism and the boundary-layer transition process.

B. Effect of different Mach numbers

When a vehicle changes its altitude within its flight corridor, its Mach number also changes. Previous research has shown that the compressible effect of increasing Mach number can alter the boundary-layer profile and stabilize it.[3] This section reports the effects of blowing control under different conditions during a wide range of flight conditions. Two sets of incoming flow conditions with different Mach numbers but the same unit Reynolds numbers and static
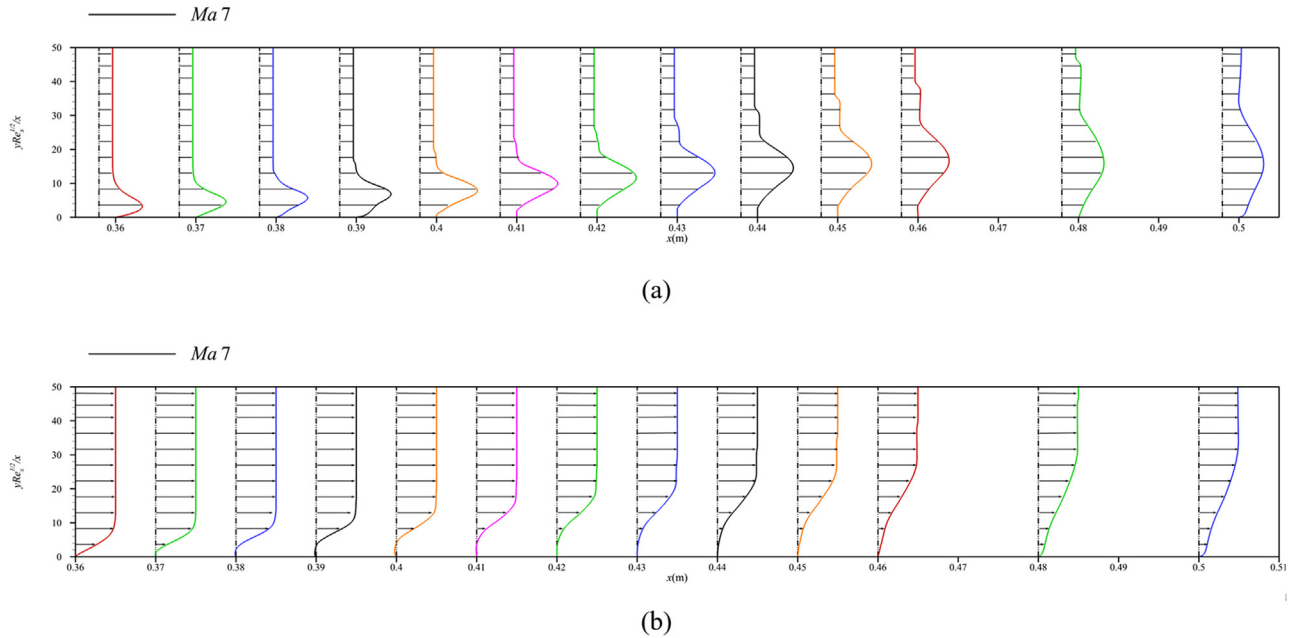
(a)

(b)

FIG. 14. Dimensionless boundary-layer profile for mass flow rate $\dot{m}_4$: (a) dimensionless temperature boundary-layer profile and (b) dimensionless streamwise velocity boundary-layer profile.
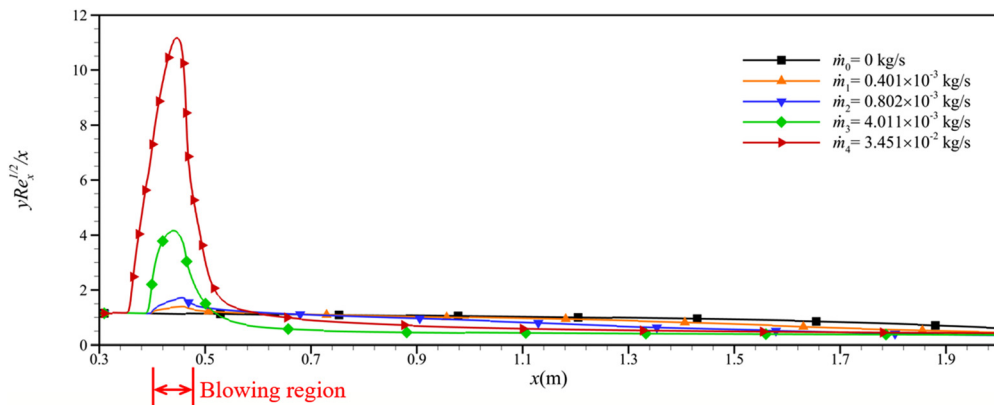

FIG. 15. Height of sonic line for various mass flow rates.

temperatures were chosen to study the impact of changing Mach number on blowing in a flat-plate boundary layer.

1. Transition characteristics

The impact of varying conditions on boundary-layer transition is first examined in light of the evolution and development of wall heat flux. Since the incoming flow conditions of the two cases are not entirely the same, a dimensionless wall heat flux is expressed using the Stanton number,

$$St = \frac{q_w}{\rho_e u_e c_p \left[T_\infty \left(1 + \frac{\gamma - 1}{2} \sqrt{\Pr} Ma_\infty^2 \right) - T_w \right]}, \quad (2)$$

where ρ_e represents the boundary-layer outer edge density, u_e represents the boundary-layer outer edge velocity, c_p represents the isobaric specific heat capacity, and Pr represents the Prandtl number.

Figure 16 shows the dimensionless wall heat flux for varying Mach numbers and blowing flow rates from $\dot{m}_0$ to $\dot{m}_2$ downstream from the blowing region. For the same blowing mass flow rate, an increase in the Mach number leads to a longer boundary-layer transition location x_{tr} and to delay the transition. For Ma 8, the transition positions of the three conditions $\dot{m}_0$-$\dot{m}_2$ all shift downstream, and the transition process on the plate is not fully developed. Since the incoming velocity of Ma 8 is slightly higher, the Stanton number in the turbulent boundary layer decreases with an increase in the Mach number. Figure 17 depicts the dimensionless wall heat flux for Ma 7 and 8 under
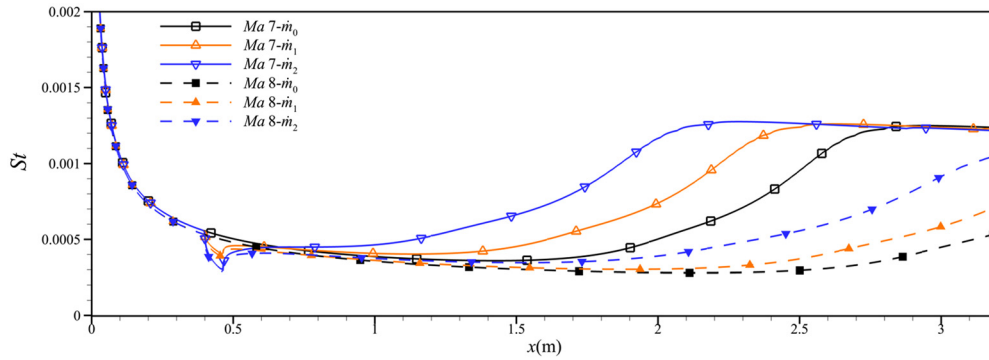
FIG. 16. Dimensionless wall heat flux for *Ma* 7 and *Ma* 8 for several low mass flow rates.
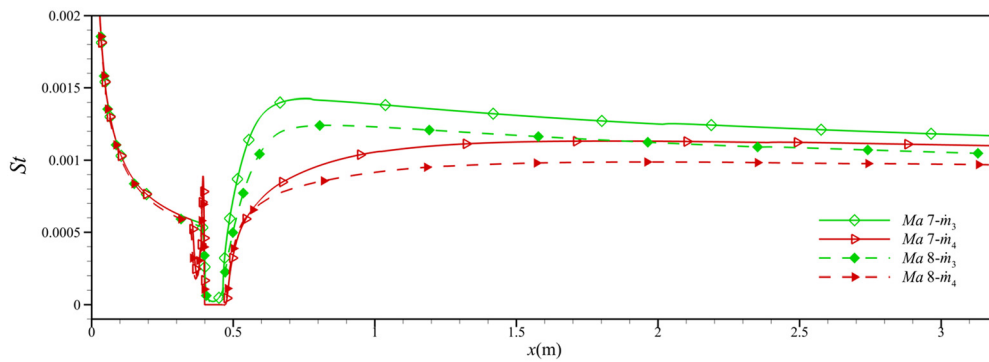

FIG. 17. Dimensionless wall heat flux for *Ma* 7 and *Ma* 8 for two high mass flow rates.

the control of blowing mass flow rates $\dot{m}_3$ and $\dot{m}_4$. As the Mach number of the incoming flow increases, the rate of increase in the heat flux downstream of the blowing region decreases. This means that the turbulent boundary layer develops more slowly, and the turbulent heat flux is less. Combining this conclusion with data in Table VI, which compares the ratio of film thickness between *Ma* 7 and 8, an increase in the Mach number of the incoming flow is seen to lead to an increase in the thickness ratio of the gas film. Due to the thicker boundary layer at higher Mach numbers, the absolute thickness of the gas film will also expand accordingly. The gas film forms a "buffer zone," delaying a change of the temperature boundary layer near the wall and reducing the wall heat flux.

The effect of Mach number on the stability of the hypersonic boundary layer can be noticed in the turbulent kinetic energy within the boundary layer. Figure 18 compares the distribution of dimensionless turbulent kinetic energy within the boundary layer at the two

TABLE VI. Gas film thickness as a percentage of boundary-layer thickness between *Ma* 7 and *Ma* 8.

Mach number	$\dot{m}_1$ (%)	$\dot{m}_2$ (%)	$\dot{m}_3$ (%)	$\dot{m}_4$ (%)
7	7.1	11.4	32.5	57.9
8	7.1	12.9	33.3	59.2

incoming flow Mach numbers 7 and 8 for natural transition conditions. The brown dot-dash line in the figure indicates the profile of the outer edge of the boundary layer. An increase in Mach number stabilizes the boundary layer. This, in turn, causes the peak value of the dimensionless turbulent kinetic energy to move downstream in the boundary layer of a flat plate without blowing control, and the region of elevated turbulent kinetic energy is seen to distances itself gradually from the wall in Fig. 18(a). The same evolutionary trend of turbulent kinetic energy is seen also in Figs. 18(b) and 18(c) with blowing control. At the same time, due to the increase in Mach number, the gradient of turbulent kinetic energy along the flow direction decreases in the region of large turbulent kinetic energy, and the peak value of turbulent kinetic energy is then reached more slowly. Increasing the Mach number elevates the boundary-layer thickness, leading to an expansion of the high turbulent kinetic energy region in the bypass transition, as illustrated in Figs. 18(c) and 18(d). However, the mechanism behind the influence of Mach number on bypass transition is more intricate.

2. Boundary-layer profile shapes

The shapes of the boundary-layer profile and subsonic region significantly impact the evolution of disturbances within the boundary layer. Figure 19 illustrates the dimensionless thickness of the boundary
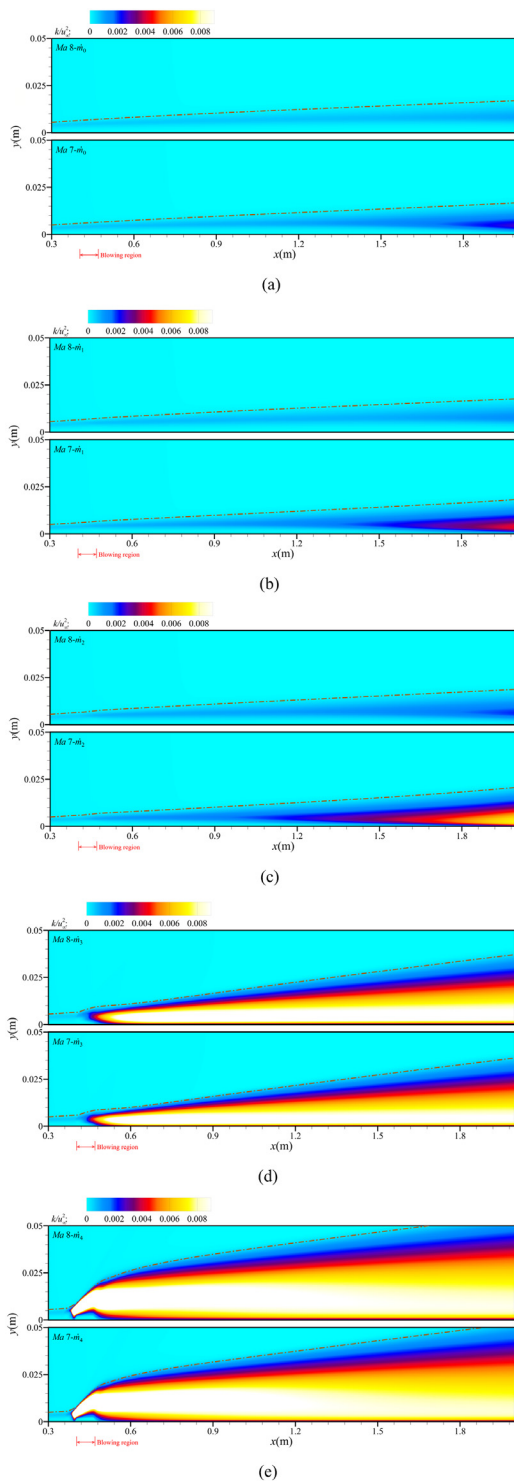
FIG. 18. Distribution of dimensionless turbulent kinetic energy within the boundary layer for *Ma* 7 and 8: (a) $\dot{m}_0 = 0$, (b) $\dot{m}_1 = 0.401 \times 10^{-3}$ kg/s, (c) $\dot{m}_2 = 0.802 \times 10^{-3}$ kg/s, (d) $\dot{m}_3 = 4.011 \times 10^{-3}$ kg/s, and (e) $\dot{m}_4 = 34.511 \times 10^{-3}$ kg/s.

layer's outer edge for each mass flow rate at incoming flow Mach numbers 7 and 8. The horizontal axis displays the position coordinate of the flat plate, while the vertical axis displays the normal coordinate following a self-similar transformation. For conditions $\dot{m}_1$ and $\dot{m}_2$ with low blowing mass flow rates, the laminar boundary-layer thickness near the blowing region increases as the incoming flow Mach number increases. Downstream of the blowing region, the *Ma* 7 condition transitions to a turbulent boundary layer earlier due to its lower Mach number. This also causes its boundary-layer thickness to gradually exceed that for *Ma* 8.

Figure 20 shows the influence of the two inflow Mach numbers and various mass flow rates on the height of the sonic line. The abscissa shows the position coordinate of the flat plate, while the ordinate shows the height of the corresponding dimensionless sonic line. An increase in Mach number results in a slower temperature change in the boundary layer and a corresponding rise in the sonic line height near the blowing region. For conditions with greater mass flow rates $\dot{m}_3$ and $\dot{m}_4$, a bypass transition is established immediately subsequent to the blowing zone and swiftly evolves into a turbulent boundary layer, resulting in an overall thickening of the boundary layer as the Mach number increases. Despite the differences in flow Mach numbers between 7 and 8, the trend of change in the height of the sonic line with the blowing mass flow rates remains nearly the same. The influence of different Mach numbers on the sonic line is concentrated mainly near the blowing area. As the Mach number increases, the sonic line of the same blowing mass flow rate experiences an increase near the blowing area. Furthermore, at a higher blowing mass flow rate, an increase in Mach number results in a corresponding rise in the increase in the sonic line. Downstream of the blowing region, due to the thickening of the boundary layer induced by an increase in Mach number, both the velocity and temperature boundary-layer profiles become more pronounced, and the height of the sonic line at high Mach numbers is generally higher than that at lower Mach numbers. However, as fully turbulent flow gradually develops, the heights of the sonic lines for different Mach numbers gradually converge, approaching that of a flat plate boundary layer devoid of outgassing.

Van Driest[52] conducted a comparative analysis of the temperature and velocity profiles of compressible laminar boundary layers at varying Mach numbers, and discovered a significant increase in boundary-layer thickness as Mach number increased. As shown in Fig. 21, the temperature and velocity patterns of the blowing boundary layer underwent changes at different Mach numbers near the blowing region with a mass flow rate of $\dot{m}_4$. In general, higher Mach number resulted in an increase in both temperature and velocity profiles. However, the elevation of the velocity profile leads to a reduction in the velocity gradient, diminishing the boundary layer's capacity to resist separation. Consequently, the *Ma* 8 condition experienced earlier boundary-layer separation and a more substantial recirculation zone upstream of the separation zone. For higher Mach number, the velocity strong-blowing layer is thicker, resulting in a lower dimensionless velocity at the same height near the wall of the blowing region. However, the higher Mach number case leads to a faster temperature rise and a larger temperature gradient above the temperature strong-blowing layer. This, in turn, results in a gradual reduction in the height of the downstream strong-blowing layer relative to that for *Ma* 7.
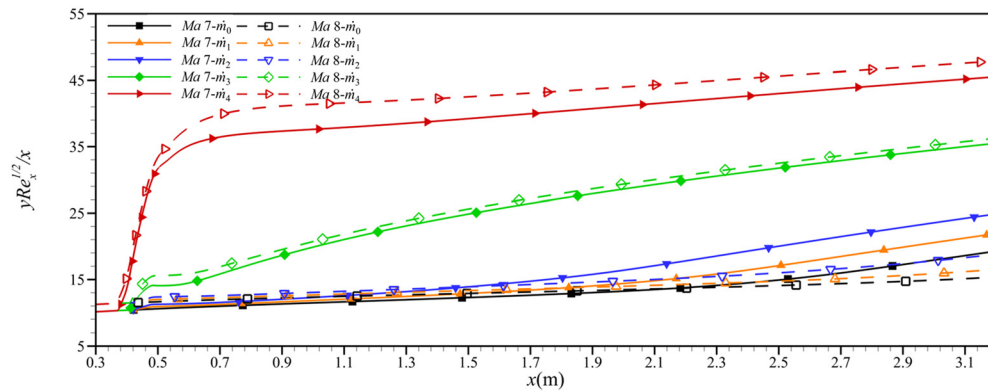
08 April 2024 03:06:28

FIG. 19. Boundary-layer thickness for Ma 7 and Ma 8 for different mass flow rates.
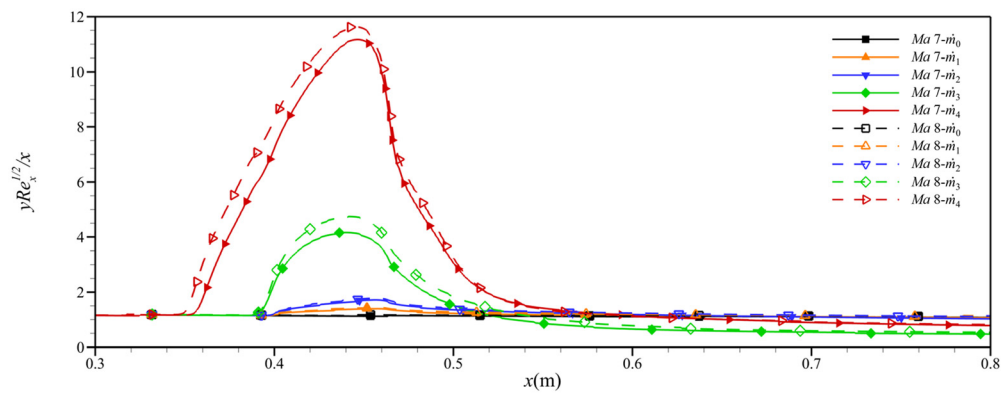

FIG. 20. Height of sonic line for Ma 7 and Ma 8 for different mass flow rates.
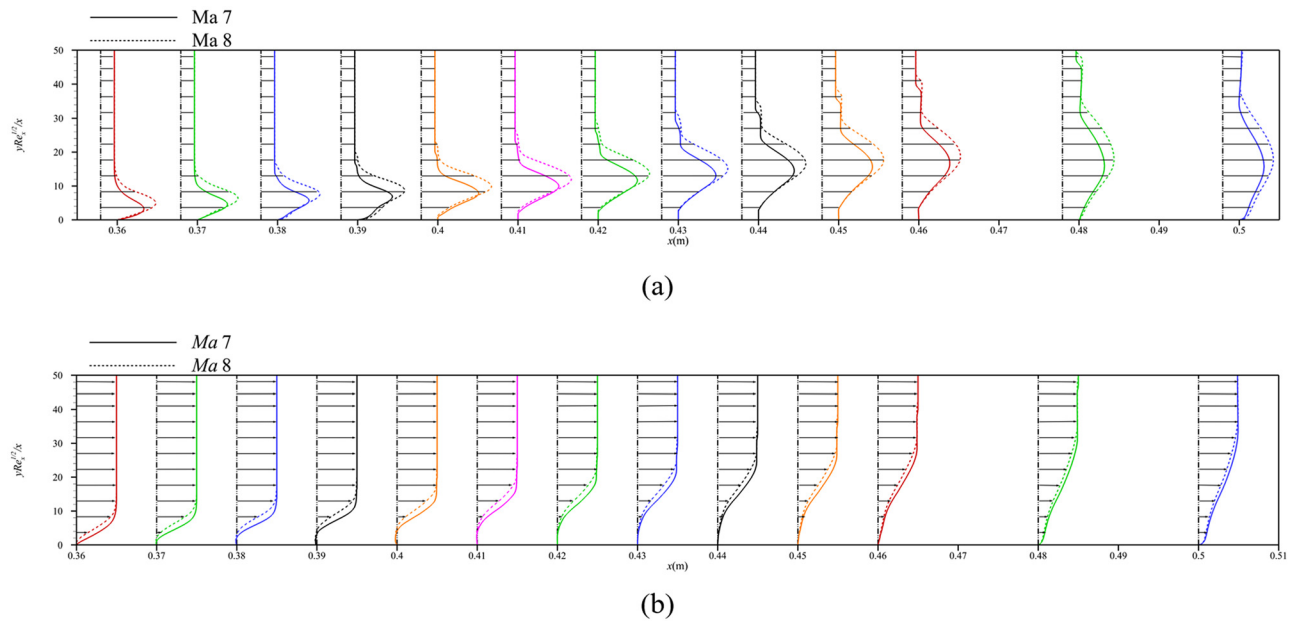

(a)

(b)

FIG. 21. Boundary-layer profiles for Ma 7 and Ma 8 at a mass flow rate of $\dot{m}_4$: (a) dimensionless temperature boundary-layer profile and (b) dimensionless streamwise velocity boundary-layer profile.

IV. CONCLUSIONS

This study employed numerical simulations to examine the impact of different incoming Mach numbers and various blowing mass flow rates on the blowing control of the hypersonic flat-plate boundary layer. The investigation focused on the evolution of the basic flow profile shape, gas film thickness, and blowing oblique shock wave intensity within the boundary layer, and compared the control effects of different flow-field parameters. The following conclusions were reached:

(1) The blowing modifies the boundary-layer profile and induces blowing oblique shock waves. Both strong-blowing layer near the blowing region and the air film downstream reduce the wall heat flux. The alterations in the blowing boundary-layer profile intensify with an increase in mass flow rate.

(2) As the mass flow rate increases, the evolution of wall heat flux characteristics indicates the promotion of transition until a bypass transition occurs. Meanwhile, the breaking position of the low intermittency factor and the peak area of turbulent kinetic energy shift to the blowing region and the recirculation zone. Which suggests that, as blowing controls the boundary-layer transition from natural to bypass, the dominant mechanism controlling instability changes.

(3) At higher Mach number, the compressibility effect becomes more pronounced, resulting in an increased thickness of the boundary layer and air film. The sonic line above the blowing area rises, expanding the subsonic region. As the Mach number increases, the boundary layer becomes more stable, the transition location and the peak region of turbulent kinetic energy are delayed under natural transition conditions.

ACKNOWLEDGMENTS

AUTHOR DECLARATIONS
Conflict of Interest

The authors have no conflicts to disclose.

Author Contributions

Zongxian Li: Conceptualization (equal); Data curation (equal); Formal analysis (equal); Investigation (equal); Methodology (equal); Resources (equal); Software (equal); Validation (equal); Visualization (equal); Writing – original draft (equal); Writing – review & editing (equal). **Meikuan Liu:** Conceptualization (equal); Data curation (equal); Formal analysis (equal); Investigation (equal); Methodology (equal); Resources (equal); Software (equal); Validation (equal); Visualization (equal); Writing – original draft (equal); Writing – review & editing (equal). **Guilai Han:** Conceptualization (equal); Data curation (equal); Formal analysis (equal); Funding acquisition (equal); Investigation (equal); Methodology (equal); Project administration (equal); Resources (equal); Software (equal); Supervision (equal); Validation (equal); Visualization (equal); Writing – original draft (equal); Writing – review & editing (equal). **Dagao Wang:** Conceptualization (equal). **Zonglin Jiang:** Conceptualization (equal).

DATA AVAILABILITY

The data that support the findings of this study are available from the corresponding author upon reasonable request.

REFERENCES

[1] P. Yu, Y. Duan, and J. Chen, "Some aerodynamic issues in hypersonic flight," Acta Aeronaut. Astronaut. Sin. **36**(1), 7 (2015).

[2] Q. Li, T. Jiang, S. Chen, Y. Chang, L. Zhao, and K. Zhang, "Measurement technique and application of boundary layer transition in shock tunnel," Acta Aeronaut. Astronaut. Sin. **40**, 122740 (2019).

[3] J. Chen, G. Tu, Y. Zhang, G. Xu, and C. Chen, "Hypersnonic boundary layer transition: What we know, where shall we go," Acta Aerodyn. Sin. **35**, 311 (2017).

[4] A. Fedorov, "Transition and stability of high-speed boundary layers," Annu. Rev. Fluid Mech. **43**, 79 (2011).

[5] L. M. Mack, "Boundary-layer linear stability theory," AGARD Report No. 709 (Jet Propulsion Laboratory, 1984), p. 1.

[6] Q. Liu, G. Tu, Z. Luo, J. Chen, R. Zhao, and X. Yuan, "Progress in hypersonic boundary layer transition delay control," Acta Aeronaut. Astronaut. Sin. **43**, 25357 (2022).

[7] W. M. F. Orr, "The stability or instability of the steady motions of a perfect liquid and of a viscous liquid. Part II: A viscous liquid," JSTOR No. 1907-69 (Royal Irish Academy, 1907).

[8] H. Schlichting and J. Kestin, *Boundary Layer Theory* (Springer, 1961).

[9] C. Lee and S. Y. Chen, "Recent progress in the study of transition in the hypersonic boundary layer," Nat. Sci. Rev. **6**, 155 (2019).

[10] M. V. Morkovin, "Transition in open flow systems-a reassessment," Bull. Am. Phys. Soc. **39**, 1882 (1994).

[11] H. Y. Men, X. L. Li, and H. W. Liu, "Direct numerical simulations of hypersonic boundary layer transition over a hypersonic transition research vehicle model lifting body at different angles of attack," Phys. Fluids **35**, 044111 (2023).

[12] X. L. Li, D. X. Fu, Y. W. Ma, and X. A. Liang, "Direct numerical simulation of compressible turbulent flows," Acta Mech. Sin. **26**, 795 (2010).

[13] X. L. Li, D. X. Fu, and Y. W. Ma, "Direct numerical simulation of hypersonic boundary layer transition over a blunt cone with a small angle of attack," Phys. Fluids **22**, 025105 (2010).

[14] X. Chen, S. W. Dong, G. H. Tu, X. X. Yuan, and J. Q. Chen, "Boundary layer transition and linear modal instabilities of hypersonic flow over a lifting body," J. Fluid Mech. **938**, A8 (2022).

[15] A. Demetriades, *Hypersonic Viscous Flow over a Slender Cone. III—Laminar Instability and Transition* (American Institute of Aeronautics and Astronautics, 1974).

[16] K. Stetson, E. Thompson, J. Donaldson, and L. Siler, "Laminar boundary layer stability experiments on a cone at Mach 8. I-sharp cone," AIAA Paper No. 83-1761, 1983.

[17] J. Jewell, R. Wagnild, I. Leyva, G. Candler, and J. Shepherd, "Transition within a hypervelocity boundary layer on a 5-degree half-angle cone in air/co_2 mixtures," AIAA Paper No. 2013-0523, 2013.

[18] J. S. Jewell, *Boundary-Layer Transition on a Slender Cone in Hypervelocity Flow with Real Gas Effects* (California Institute of Technology, 2014).

[19] M. K. Liu, G. L. Han, and Z. L. Jiang, "Experimental study on the evolution of mode waves in laminar boundary layer on a large-scale flat plate," Phys. Fluids **34**, 013612 (2022).

[20] M. K. Liu, G. L. Han, Z. X. Li, and Z. L. Jiang, "Experimental study on the effects of the cone nose-tip bluntness," Phys. Fluids **34**, 101703 (2022).

[21] Z. Li, H. Yuan, B. Huang, Z. Zhang, and X. Yu, "The hypersonic boundary-layer transition: A perspective from the view of system design," Acta Aerodyn. Sin. **39**, 26 (2021).

[22] G. P. Camillo, A. Wagner, C. Dittert, L. Benjamin, V. Wartemann, J. Neumann, and R. Hink, "Experimental investigation of the effect of transpiration cooling on second mode instabilities in a hypersonic boundary layer," Exp. Fluids **61**, 162 (2020).

[23] D. W. Bogdanoff, "Advanced injection and mixing techniques for scramjet combustors," J. Propul. Power **10**, 183 (1994).

[24] W. Huang, H. Wu, Y. G. Yang, L. Yan, and S. B. Li, "Recent advances in the shock wave/boundary layer interaction and its control in internal and external flows," Acta Astronaut. **174**, 103 (2020).

[25] H-s Yang, H. Liang, S-g Guo, M-x Tang, C-b Zhang, Y. Wu, and Y-h Li, "Research progress of hypersonic boundary layer transition control experiments," Adv. Aerodyn. **4**(1), 18 (2022).

[26] F. M. Miro and F. Pinna, "Injection-gas-composition effects on hypersonic boundary-layer transition," J. Fluid Mech. **890**, R4 (2020).

[27] S. P. Schneider, "Hypersonic boundary-layer transition with ablation and blowing," J. Spacecr. Rockets **47**, 225 (2010).

[28] B. E. Schmidt, N. P. Bitter, H. G. Hornung, and J. E. Shepherd, "Injection into supersonic boundary layers," AIAA J. **54**, 161 (2016).

[29] A. V. Fedorov, V. Soudakov, and I. A. Leyva, "Stability analysis of high-speed boundary-layer flow with gas injection," AIAA Paper No. 2014-2498, 2014.

[30] R. H. M. Giepman, F. F. J. Schrijer, and B. W. Van Oudheusden, "Flow control of an oblique shock wave reflection with micro-ramp vortex generators: Effects of location and size," Phys. Fluids **26**, 066101 (2014).

[31] X. Wu and M. Dong, "A local scattering theory for the effects of isolated roughness on boundary-layer instability and transition: Transmission coefficient as an eigenvalue," J. Fluid Mech. **794**, 68 (2016).

[32] W. K. Zhu, X. Chen, Y. D. Zhu, and C. B. Lee, "Nonlinear interactions in the hypersonic boundary layer on the permeable wall," Phys. Fluids **32**, 104110 (2020).

[33] A. Fedorov, V. Soudakov, I. Egorov, A. Sidorenko, D. Gromyko, D. Bountin, P. Polivanov, and A. Maslov, "High-speed boundary-layer stability on a cone with localized wall heating or cooling," AIAA J. **53**, 2512 (2015).

[34] H. Jiang, J. Liu, S. C. Luo, J. Y. Wang, and W. Huang, "Hypersonic flow control of shock wave/turbulent boundary layer interactions using magnetohydrodynamic plasma actuators," J. Zhejiang Univ. Sci. A **21**, 745 (2020).

[35] T. M. Reedy, N. V. Kale, J. C. Dutton, and G. S. Elliott, "Experimental characterization of a pulsed plasma jet," AIAA J. **51**, 2027 (2013).

[36] K. S. Aley, T. K. Guha, and R. Kumar, "Active flow control of a high-lift supercritical airfoil with microjet actuators," AIAA J. **58**, 2053 (2020).

[37] D. Tang, *Boundary Layer Transition* (Science Press, 2015).

[38] C. C. Pappas and A. F. Okuno, *Heat-Transfer Measurement for Binary Gas Laminar Boundary Layers with High Rates of Injection* (National Aeronautics and Space Administration, 1964).

[39] A. Demetriades, A. J. Laderman, L. Von Seggern, A. T. Hopkins, and J. C. Donaldson, "Effect of mass addition on the boundary layer of a hemisphere at Mach 6," J. Spacecr. Rockets **13**, 508 (1976).

[40] R. B. Langtry and F. R. Menter, "Correlation-based transition modeling for unstructured parallelized computational fluid dynamics codes," AIAA J. **47**, 2894 (2009).

[41] K. Bensassi, A. Lani, and P. Rambaud, "Numerical investigations of local correlation-based transition model in hypersonic flows," AIAA Paper No. 2012-3151, 2012.

[42] W. Kong, C. Yan, and R. Zhao, "γ-Re_θ model research for high-speed boundary layer transition," Acta Aerodyn. Sin. **31**, 120 (2013).

[43] Z. Zheng, H. Y. Li, and D. X. Liu, "Application and analysis of γ-Re_θ transition model in hypersonic flow," J. Propul. Technol. **35**, 296 (2014).

[44] H. Yang, W. Lu, H. Li, and L. Yue, "Hypersonic air inlet performance based on engineering transition model," J. Beijing Univ. Aeronaut. Astronaut. **44**, 1408 (2018).

[45] G. Cheng, R. Nichols, K. Neroorkar, and P. Radhamony, *Validation and Assessment of Turbulence Transition Models* (American Institute of Aeronautics and Astronautics, 2009).

[46] R. Mao, P. Yan, and X. Qiang, "Application of PSE analysis method with transitional turbulence model on hypersonic flows," AIAA Paper No. 2011-3981, 2011.

[47] Y. Zhang, K. He, Y. Zhang, M. Mao, and J. Chen, "Improvement and validation of Menter's transition model for hypersonic flow simulation," J. Astronaut. **37**, 397 (2016).

[48] J. D. Anderson, *Hypersonic and High Temperature Gas Dynamics* (AIAA, 1989).

[49] J. Ou, B. Wan, J. Liu, and W. Cao, "Basic flow characteristics in entropy layer of hypersonic flow around blunt body," Acta Aerodyn. Sin. **36**, 238 (2018).

[50] F. M. Miro, P. Dehairs, F. Pinna, M. Gkolia, D. Masutti, T. Reger, and O. Chazot, "Effect of wall blowing on hypersonic boundary-layer transition," AIAA J. **57**, 1567 (2019).

[51] R. A. Humble, S. J. Peltier, and R. D. W. Bowersox, "Visualization of the structural response of a hypersonic turbulent boundary layer to convex curvature," Phys. Fluids **24**, 106103 (2012).

[52] E. van Driest, "Investigation of laminar boundary layer in compressible fluid using the Crocco method," NACA TN 2597 10 (UNT Digital Library, 1952).

08 April 2024 03:06:28